

Excited-State Studies of Polyacenes: A Comparative Picture Using EOMCCSD, CR-EOMCCSD(T), Range-Separated (LR/RT)-TDDFT, TD-PM3, and TD-ZINDO

K. Lopata,^{*,†} R. Reslan,[‡] M. Kowalska,[§] D. Neuhauser,^{*,‡} N. Govind,^{*,†} and K. Kowalski^{*,†}

[†]William R. Wiley Environmental Molecular Sciences Laboratory, Pacific Northwest National Laboratory, Richland, Washington 99352, United States

[‡]Department of Chemistry and Biochemistry, University of California, Los Angeles, California 90095-1569, United States

[§]Department of Chemistry, Washington State University Tri-Cities, Richland, Washington 99354, United States

ABSTRACT: The low-lying excited states (L_a and L_b) of polyacenes from naphthalene to heptacene ($N = 2-7$) are studied using various time-dependent computational approaches. We perform high-level excited-state calculations using equation of motion coupled cluster with singles and doubles (EOMCCSD) and completely renormalized equation of motion coupled cluster with singles, doubles, and perturbative triples (CR-EOMCCSD(T)) and use these results to evaluate the performance of various range-separated exchange-correlation functionals within linear-response (LR) and real-time (RT) time-dependent density functional theories (TDDFT). As has been reported recently, we find that the range-separated family of functionals addresses the well-documented TDDFT failures in describing these low-lying singlet excited states to a large extent and are as accurate as results from EOMCCSD on average. Real-time TDDFT visualization shows that the excited state charged densities are consistent with the predictions of the perimeter free electron orbital (PFE0) model. This corresponds to particle-on-a-ring confinement, which leads to the well-known red-shift of the excitations with acene length. We also use time-dependent semiempirical methods like TD-PM3 and TD-ZINDO, which are capable of handling very large systems. Once reparametrized to match the CR-EOMCCSD(T) results, TD-ZINDO becomes roughly as accurate as range-separated TDDFT, which opens the door to modeling systems such as large molecular assemblies.

1. INTRODUCTION

Polyacenes or acenes constitute a class of polycyclic organic compounds consisting of linearly fused benzene rings. These compounds, and their derivatives, have been studied extensively, and over the last several years, the larger representatives in this class have been used in a plethora of applications such as light-emitting diodes,¹⁻⁴ photovoltaic cells,⁵⁻⁷ liquid crystal displays,⁸ and organic field-effect transistors^{9,10} to name a few. Pentacene, in particular, has received much attention because of its high charge-carrier (hole) mobility in films and molecular crystals.¹¹⁻¹³ For an overview of the electronic applications of acenes, see the reviews by Anthony.^{14,15}

In a nutshell, the electronic properties of these materials are dictated by the π electrons which occupy the highest occupied and lowest unoccupied states; the π interactions between adjacent acene molecules, for example, give rise to the high hole mobility through molecular films. In a single molecule, the lowest valence excitations have $\pi-\pi^*$ character, and the two lowest singlet excitations are commonly assigned as the L_a (B_{2u} symmetry) and L_b (B_{3u} symmetry) states, respectively. The former represents the polarization along the short axis, while the latter represents the polarization along the long axis. The L_b is the lowest excited state in naphthalene but switches positions with the L_a state for larger acenes, with the crossing happening around anthracene. It has long been suggested, from a valence-bond point of view, that the L_a state is mostly ionic in character involving significant rearrangement of the excited-state density, whereas the L_b state is mostly covalent where the excited-state density is similar to the ground state.

There has been significant progress in describing these excitations theoretically,¹⁶⁻²³ within which time-dependent

density functional theory (TDDFT)²⁴⁻²⁶ has been the predominant method. It is now well-known, however, that for TDDFT traditional and global hybrid functionals fail to describe these lowest excitations. Grimme and Parac demonstrated that the ordering switches earlier than expected with both classes of functionals, and the excitation energy of the L_a state is severely underestimated and progressively worsens with system size.²⁰ Increasing the Hartree-Fock (HF) content in the exchange-correlation improves the picture, but L_a worsens the excitation energy of the L_b state. They concluded that it was impossible to capture both states accurately just by adjusting the HF content.

Very recently, range-separated hybrid (RSH) functionals have been applied to the L_a state in acenes.^{17-19,22} RSHs correct the incorrect asymptotic behavior of the exchange by splitting the exchange into a short-range part and a long-range part. For many optically active charge transfer states, RSHs rival the accuracy of the equation of motion coupled cluster singles doubles (EOMCCSD) method on average. The success of RSHs in this case, however, is in many ways quite surprising, as the L_a state is an intramolecular transverse excitation (along short-axis of molecule) and clearly not long-range at all. Richard and Herbert labeled this a charge-transfer-like state in disguise,¹⁸ which Kuritz et al. subsequently rationalized as arising from minimal overlap in auxiliary orbitals,¹⁹ akin to minimal overlap of the hole/charge orbitals in a typical charge transfer excitation.

Received: July 26, 2011

Published: September 14, 2011

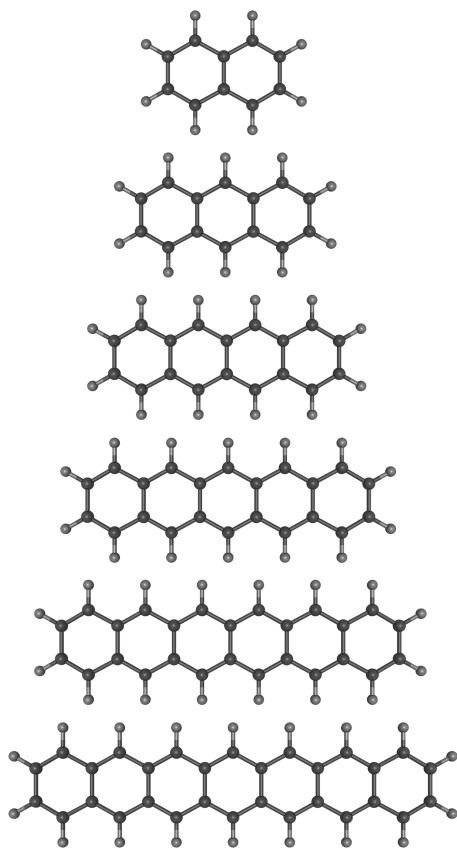


Figure 1. Structures of the acenes studied. From top to bottom: naphthalene ($N = 2$), anthracene ($N = 3$), tetracene ($N = 4$), pentacene ($N = 5$), hexacene ($N = 6$), heptacene ($N = 7$).

In some sense, acenes serve as a rough prototype for a more complicated light harvesting system and also as the fundamental building block for many molecular electronic devices. Careful analysis of the excitations in these deceptively simple molecules serves as a crucial test for the accuracy and predictive power of a theoretical technique, as indicated by the intense interest in benchmarking TDDFT results in these systems. In this light, our main goal in this paper is to examine the low-lying excited states of polyacenes from naphthalene to heptacene (Figure 1) using a wide selection of time-dependent approaches. We first perform a systematic analysis based on high-level coupled cluster (EOMCCSD and CR-EOMCCSD(T)) calculations. These calculations are used to benchmark the performance of various range-separated exchange-correlation functionals implemented within linear response and real-time TDDFT. Additionally, we explore the use of semiempirical time-dependent PM3 and ZINDO for describing these excitations and reparametrize their Hamiltonians to better match the results of high level theory. All structures were obtained using cc-pVTZ/B3LYP.

The rest of the paper is organized as follows: In section 2, we briefly review the various time-dependent approaches used in this study and provide the necessary computational details. The results are presented and discussed in section 3 and the concluding remarks in section 4.

2. METHODOLOGIES AND COMPUTATIONAL DETAILS

Below, we briefly review the formalisms for equation of motion coupled cluster (EOMCC), real-time time-dependent density

functional theory (RT-TDDFT), and real-time time-dependent PM3 and ZINDO. All results except the PM3 and ZINDO ones were obtained using NWChem.²⁷ The TD-PM3 results were obtained by a modification of the PM3 module from MOPAC 6.0,^{28,29} to perform iterative time-dependent calculation of the TD-PM3 excitation energies.³⁰ The TD-ZINDO results were obtained by an analogous modification of ZINDO from the ZINDO-MN package.³¹ The linear response TDDFT results were calculated using the module in NWChem; since the approach is widely used (e.g., refs 26 and 32), we omit the details.

2.1. Equation of Motion Coupled Cluster. The EOMCC formalism³³ can be viewed as an excited-state extension of the single-reference coupled cluster method, where the wave function corresponding to the K th state is represented as

$$|\Psi_K\rangle = R_K e^T |\Phi\rangle \quad (1)$$

where T and state-specific R_K operators are the cluster and excitation operators, respectively, and $|\Phi\rangle$ is the so-called reference function usually chosen as a Hartree–Fock determinant. Various approximate schemes range from the basic EOMCCSD approximation where the cluster and correlation operators are represented as sums of scalar ($R_{K,0}$ for excitation operator only), single ($T_1, R_{K,1}$), and double ($T_2, R_{K,2}$) excitations

$$|\Psi_K^{\text{EOMCCSD}}\rangle = (R_{K,0} + R_{K,1} + R_{K,2}) e^{T_1 + T_2} |\Phi\rangle \quad (2)$$

to the more advanced EOMCCSDT and EOMCCSDTQ approach, accounting for the effect of triple and/or quadruple excitations. It has been demonstrated that the progression of methods, EOMCCSD \rightarrow EOMCCSDT \rightarrow EOMCCSDTQ..., in the limit converges to the exact (full configuration interaction) energies. However, the rapid growth in the numerical complexity of the EOMCC methods makes calculations with the EOMCCSDT or EOMCCSDTQ methods very expensive, even for relatively small systems. Unfortunately, the EOMCCSD method is capable of providing reliable results only for singly excited states. However, as has recently been demonstrated,³⁴ errors in the range of 0.25–0.30 eV with respect to the experimental vertical excitation energies (VEE) persist with increasing system size.

In order to narrow the gap between the EOMCCSD and EOMCCSDT VEEs, several noniterative N^7 -scaling methods that mimic the effect of triples in a perturbative fashion have been proposed in the past.^{35–40} The completely renormalized EOMCCSD(T) approach, denoted CR-EOMCCSD(T),⁴¹ falls into this class (see also refs 42 and 43–45 for the most recent developments). In this approach, the energy correction $\delta_K^{\text{CR-EOMCCSD(T)}}$ is added to the EOMCCSD VEE ($\omega_K^{\text{EOMCCSD}}$)

$$\omega_K^{\text{CR-EOMCCSD(T)}} = \omega_K^{\text{EOMCCSD}} + \delta_K^{\text{CR-EOMCCSD(T)}} \quad (3)$$

where $\delta_K^{\text{CR-EOMCCSD(T)}}$ is expressed through the trial wave function $\langle\Psi_K|$ and the triply excited EOMCCSD moment operator $M_{K,3}^{\text{EOMCCSD}}$ (see ref 41 for details):

$$\delta_K^{\text{CR-EOMCCSD(T)}} = \frac{\langle\Psi_K|M_{K,3}^{\text{EOMCCSD}}|\Phi\rangle}{\langle\Psi_K|(R_{K,0} + R_{K,1} + R_{K,2}) e^{T_1 + T_2}|\Phi\rangle} \quad (4)$$

Although the CR-EOMCCSD(T) method is characterized by the same N^7 scaling as the ground-state CCSD(T) method,⁴⁶ the fact that triply excited EOMCCSD moments need to be calculated makes this approach a few times more expensive than the ground-state CCSD(T) approach.

2.2. Real-Time TDDFT. In real-time time-dependent density functional theory (RT-TDDFT), the time-dependent Kohn–Sham (KS) equations are explicitly propagated in time:

$$i \frac{\partial \psi_i(\mathbf{r}, t)}{\partial t} = \left[-\frac{1}{2} \nabla^2 + v_{\text{KS}}[\rho](\mathbf{r}, t) \right] \psi_i(t) \quad (5)$$

$$= \left[-\frac{1}{2} \nabla^2 + v_{\text{ext}}(\mathbf{r}, t) + v_{\text{H}}(\mathbf{r}, t) + v_{\text{XC}}[\rho](\mathbf{r}, t) \right] \psi_i(t) \quad (6)$$

where $\rho(\mathbf{r}, t)$ is the charge density, $v_{\text{ext}}(\mathbf{r}, t)$ is the external potential describing the nuclear–electron and applied field contributions, $v_{\text{H}}(\mathbf{r}, t)$ is the electron–electron potential, and $v_{\text{XC}}[\rho](\mathbf{r}, t)$ is the exchange–correlation potential, which is henceforth assumed to depend only on the instantaneous density (adiabatic approximation). In a Gaussian-orbital basis, it is simpler to work with density matrices rather than KS orbitals, in which case the evolution of the electronic density is governed by the von Neumann equation:

$$i \frac{\partial \mathbf{P}'}{\partial t} = [\mathbf{F}'(t), \mathbf{P}'(t)] \quad (7)$$

where the prime notation denotes matrices in the orthogonal molecular orbital (MO) basis and unprimed denotes matrices in the atomic orbital (AO) basis. Note that in eq 7, all matrices are complex quantities. The Fock matrix $\mathbf{F}(t)$ is computed in the AO basis similar to ground state DFT, with the important distinction that in the absence of Hartree–Fock exchange (e.g., pure DFT); $\mathbf{F}(t)$ is real symmetric and only depends on the real part of $\mathbf{P}(t)$. If HF exchange is included (e.g., hybrid functionals), it becomes complex Hermitian (see ref 47 for details of the NWChem RT-TDDFT implementation, derivations, and references).

There are numerous approaches taken to propagate eq 7. In this study, we use a second order Magnus scheme, which is equivalent to an exponential midpoint propagator

$$\mathbf{P}'(t + \Delta t) = e^{-i\mathbf{F}'(t + \Delta t/2)\Delta t} \mathbf{P}'(t) e^{i\mathbf{F}'(t + \Delta t/2)\Delta t} \quad (8)$$

where we compute the Fock matrix at the future time via linear extrapolation from the previous two values, followed by iterative interpolation until converged. This approach is extremely stable, as it maintains the idempotency of the density matrix and yields order $(\Delta t)^2$ accuracy. In practice, this allows for time steps on the order of $\Delta t = 0.1 \text{ au} = 2.42 \times 10^{-3} \text{ fs}$ with a minimal loss of accuracy. The exponentiation of eq 8 is done via contractive power series, where the operator is first divided by 2^m such that the norm of the scaled operator is less than 1, performing the power series (which is guaranteed to converge well numerically since it is contractive), then squaring the result m times to recover the result. All real-time TDDFT simulations here used a time step of $\Delta t = 0.2 \text{ au} = 0.0048 \text{ fs}$ and ran up to $1500 \text{ au} = 36.3 \text{ fs}$, which corresponds to 7500 time steps.

To obtain spectroscopic information, the system is excited via a linearly polarized (x, y, z) narrow Gaussian electric field kick, which adds to the Fock matrix via dipole coupling:

$$\mathbf{E}(t) = \kappa \exp[-(t - t_0)^2/2w^2] \hat{\mathbf{d}} \quad (9)$$

where $\hat{\mathbf{d}} = \hat{x}, \hat{y}, \hat{z}$ is the polarization, κ is the field maximum (dimensions of electric field), t_0 is the center of the pulse, and w is the width, which is typically $\sim \Delta t$. This induces all electronic modes simultaneously, and the Fourier transform of the resulting

time-dependent dipole moment yields the absorption spectrum for that polarization. The sum of the three spectra gives the full absorption. In the limit of a small electric field perturbation, real-time TDDFT and linear-response yield essentially identical spectroscopic results. Unlike LR-TDDFT, RT-TDDFT is also valid in the strong perturbation regime, but the studies presented here are all the weak-field type and thus comparable to LR-TDDFT. All kick-type results here used a kick with $\kappa = 0.002 \text{ au} = 1.0 \text{ V/nm}$, $t_0 = 3.0 \text{ au} = 0.07 \text{ fs}$, and $w = 0.2 \text{ au} = 0.0048 \text{ fs}$.

The true power of RT-TDDFT, however, lies in direct modeling of the electron dynamics in response to a realistic stimulus, such as a laser tuned to resonance with a particular electronic transition. For example, to excite the system into a particular state of interest, it is simplest to use a Gaussian enveloped monochromatic laser pulse of the form:

$$\mathbf{E}(t) = \kappa \exp[-(t - t_0)^2/2w^2] \cos(\omega_0 t) \hat{\mathbf{d}} \quad (10)$$

where ω_0 is the driving frequency and w is broad enough to encapsulate at least a few oscillations. In this case, the charge density can be visualized in 4D (three space + time), which yields detailed insight into the fundamental nature of the excitation. This is especially important as an intuitive metric for characterizing charge transfer excitations, and when elucidating the mechanism of excitations. In this paper, RT-TDDFT is used as a visual tool to assign longitudinal and transverse excitations into two distinct classes (ionic vs covalent, respectively) and to study the physical origin of the red-shift with acene length.

2.3. Time-Dependent Semiempirical Methods. A well-known alternative to first-principles approaches is semiempirical methods (e.g., PM3²⁸ and ZINDO⁴⁸) which can be extended to a time-dependent formalism.³⁰ A minimal valence basis set is used, so that there are only four orbitals for each carbon atom. Typically, the Fock matrix has the generic Hartree–Fock-like form:

$$F_{ij} = h_{ij} + \sum_{kl} v_{ijkl} P_{ij} \quad (11)$$

where h_{ij} and v_{ijkl} are semiempirical one-body and interaction parameters, respectively. Unlike Hartree–Fock and DFT, however, the interaction parameters are restricted to be at most two-center. The calculations are done in an atomic basis (rather than molecular orbital basis, which earlier TD-semiempirical methods use) so that the calculation of the Fock matrix scales like N^2 , where N is the number of orbitals.

After the initial SCF solution labeled as P_0 , the same von Neumann equation as in TDDFT (eq 7) is propagated. While the same real-time approach as in eq 8 could have been used, here, however a different algorithm is found to be more efficient. The algorithm has been covered recently (see ref 30), so it will only be briefly reviewed. Basically, the linear-response von Neumann operator is constructed:

$$LZ \equiv \frac{dZ}{dt} = -i \frac{[F(P_0 + \eta Z), P_0 + \eta Z] - [F(P_0), P_0]}{\eta} \quad (12)$$

for the deviation from the initial density matrix:

$$Z \equiv \mathbf{P} - P_0 \quad (13)$$

and η is a small parameter ensuring linearity. Then, the time-dependent dynamics are represented by writing a Chebyshev

algorithm for the propagator:

$$\mathbf{Z}(t) = e^{Lt} \mathbf{Z}_0 = \sum_n (2 - \delta_{n0}) J_n(t\Delta H) T_n \left(\frac{L}{\Delta H} \right) \mathbf{Z}_0 \quad (14)$$

where we introduced the Bessel and modified Chebyshev operators, with the latter propagated as

$$T_n \left(\frac{L}{\Delta H} \right) \mathbf{Z}_0 = 2 \frac{L}{\Delta H} T_{n-1} \left(\frac{L}{\Delta H} \right) \mathbf{Z}_0 + T_{n-2} \left(\frac{L}{\Delta H} \right) \mathbf{Z}_0 \quad (15)$$

and

$$\mathbf{Z}_0 = -i[\mathbf{D}, \mathbf{P}_0] \quad (16)$$

where \mathbf{D} is the dipole moment matrix. ΔH is half the spectrum width, so that $(\Delta H)^{-1}$ is the effective time-step; it is quite large (almost 0.4 au), so that the overall number of iterations required is quite small (a few thousands even without any signal processing approaches). This approach minimizes the number of matrix multiplications, which in semiempirical calculations are the most time-consuming steps (scales as N^3 unless sparse matrix algorithms are used). Further savings are obtained by Fourier transforming the time-dependent Bessel function coefficients in eq 14 analytically, thereby reducing the required number of iterations. As with RT-TDDFT, spectroscopic information is obtained via kick-type excitations.

3. RESULTS

In this section, we present acene vertical excitation energies (VEEs) for a wide range of theories: coupled cluster (EOMCCSD, CR-EOMCCSD(T)), linear response TDDFT with a global hybrid functional (B3LYP⁴⁹) and a variety of range-separated functionals (CAM-B3LYP,⁵⁰ LC-BLYP, LC- ω PBE,⁵¹ BNL⁵²), real-time TDDFT with the BNL functional, and two semiempirical methods (TD-ZINDO, TD-PM3). Before discussing results, it is important to note that vertical excitation energies, which correspond to the energy difference between ground and excited states without a change in geometry, cannot be directly measured experimentally (see ref 21). As a good approximation, VEEs can be measured experimentally via the locations of experimental UV–vis absorption peaks, but the accuracy of this approximation varies depending on state and molecule, with deviations typically on the order of a few tenths of an electronvolt. To ensure meaningful comparisons between the computed VEEs and experimental results, we use the corrected acene experimental values from Grimme and Parac²⁰ (see ref 53 for the original experimental results). In a nutshell, these incorporate adjustments to the L_a and L_b states computed from TDDFT (B3LYP/TZVP) excitation energies with fully optimized excited state geometries (calculated for acenes $N = 2, 3, 4$; extrapolated to $N = 5, 6, 7$). This somewhat accounts for geometry relaxation effects, but significant theory–experiment discrepancies still arise from basis set quality and the level of theory, specifically the treatment of correlation effects.

The L_a and L_b vertical excitation energies for the set of acenes are summarized in Table 1, along with the corrected experimental values, and the mean average error (MAE) from the experiment, for the full set of acenes for each approach. These VEEs (for a few representative theories) are plotted against acene size in Figure 4. Qualitatively speaking, all methods capture most of the gross features, including the red-shift of the L_b (longitudinal) state with acene length and the steeper red-shift of the L_a (transverse) state with acene length. However, there is only mixed success in

describing the important experimentally observed crossover of the lowest energy state from $L_a \rightarrow L_b$ around anthracene; this is discussed in more detail below.

3.1. Equation-of-Motion Coupled Cluster. Overall, CR-EOMCCSD(T) has the best agreement with experimental energies, with a MAE of 0.07 eV for the L_a state and 0.06 eV for the L_b . Most importantly, CR-EOMCCSD(T) simultaneously describes both states well and captures the crossover at the right energy (near anthracene). That is, it predicts that L_a is lower in energy than L_b for naphthalene. They are roughly equal for anthracene, and L_b is lower afterwards (see Figure 2). In contrast to the experimental vertical excitation energies, the EOMCCSD and CR-EOMCCSD(T) approaches predict for anthracene the reversed ordering of the L_a and L_b states. The CR-EOMCCSD(T) excitation energy for the L_b state is located 0.1 eV below the one corresponding to the L_a state. Similar reverse ordering has been reported in the context of multireference Møller–Plesset (MRPT) theory^{54,55} calculations for low-lying excited states of anthracene.¹⁶ In the case of the MRPT approach, the 0.17 eV separation between L_b and L_a states is slightly larger than 0.1 eV obtained with the CR-EOMCCSD(T) method for POL1 basis set. The CC2 model,⁵⁶ which is an approximation to the EOMCCSD formalism, predicts the L_a state to the lowest state, and the calculated separation between L_a and L_b states is around 0.2 eV.

3.2. Linear Response TDDFT. The range-separation parameter for the CAM-B3LYP,⁵⁰ LC-BLYP, and BNL⁵² functionals was taken to be 0.33 au⁻¹; for LC- ω PBE,⁵¹ it was 0.30 au⁻¹. For the transverse charge-transfer-like L_a state (solid lines in Figure 2), all of the range-separated TDDFT results agree well with experimental results and EOMCC, with MAE typically around a few hundredths of an electronvolt. Real-time BNL results are essentially the same as the corresponding linear response ones, since the kick perturbation was small. Range-corrected TDDFT is less accurate for the L_b state, however, with MAEs of ~ 0.3 eV, which is almost twice that of B3LYP. Thus, range-separated TDDFT excels at predicting the challenging charge-transfer-like L_a state, but using a range-separated functional significantly compromises the accuracy of the L_b state versus a global hybrid approach (e.g., B3LYP). To better understand the accuracy of RSH functionals, two versions of the CAM-B3LYP functional were studied: The first, denoted “CAM-B3LYP (I)”, has an asymptote of 0.65/ r (i.e., $\alpha + \beta = 0.65$), while the second, denoted “CAM-B3LYP (II)”, has an asymptote of 1.0/ r . The full Hartree–Fock asymptote in the exchange in CAM-B3LYP (II) improves the accuracy in the L_a state at a cost of slightly decreasing the accuracy of the L_b state. On another note, range-separated TDDFT correctly predicts the $L_a \rightarrow L_b$ crossover (intersection of like-colored solid and dashed lines in Figure 2), albeit at a lower energy than the experiment. B3LYP, in contrast, fails to even qualitatively capture this crossover. In short, using range-separated functionals overcomes many of the failures of pure or hybrid DFT functionals in describing the transverse L_a state and the $L_a \rightarrow L_b$ crossover, with overall accuracy rivaling that of CC2. The use of “tuned” RSHs, which has been pioneered by Baer and co-workers,⁵⁷ shows promise in further improving the accuracy of TDDFT for systems such as this.¹⁹

3.3. Time-Dependent PM3 and ZINDO. We performed time-dependent simulations with two typical semiempirical methods, PM3 and ZINDO. The latter is well-known to be better for spectra, as our results indicate. In order to parametrize the TD-ZINDO approach against the coupled CR-EOMCCSD(T) results for the charge-transfer-like L_a , we scaled down the strength of the $\pi\pi'$ interaction potentials, as is commonly done in ZINDO. We

Two distinct mechanisms of excitation are clearly visible in Figure 4. The longitudinally excited charge density (B_b state; top) sloshes back and forth along the π^* orbitals along the acene backbone; at the extrema, the charge density has piled up at one end of the molecule, with corresponding depletion (hole) on the opposite end. After transverse excitation (L_a state; bottom), however, the density is driven from delocalized π orbitals across

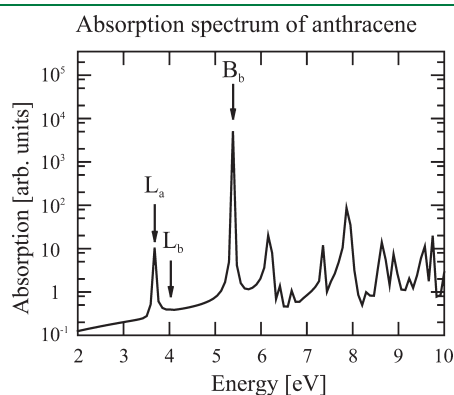


Figure 3. Absorption spectrum of anthracene ($N = 3$) obtained via RT-TDDFT (POLI/BNL). The bright L_a and dim L_b peaks correspond to transverse and longitudinal excitations, respectively. The intensely bright longitudinal UV B_b peak is visualized in Figure 4 but not compared in Table 1.

the acene and forced to populate the orbitals above and below the C–H bonds, which leads to alternating “fingers” of accumulated charge, and thus alternating $\cdots C^{\delta+}C^{\delta-}C^{\delta+}C^{\delta-} \cdots$ atoms along the acene. In a valence bond picture, this is an ionic-like excitation, in agreement with previous analyses.^{18,20} The intramolecular charge-transfer-like character (or charge transfer in disguise) is not due to a long-range pileup of charge but instead arises from this ionic-like character. Here, range-separated functionals perform well because they are able to capture interaction between these regions of alternating charge and hole. This is related to Kuritz et al.’s discussion, where a state is characterized as charge-transfer-like on the basis of minimal overlap of auxiliary orbitals.¹⁹

RT-TDDFT can also shed light on the origin of the red shifts. As the acenes increase in length, the time taken to oscillate increases (frequency decreases) for both the transverse and longitudinal excitations. Although not immediately obvious, the red shifts of both excitations can be rationalized in a similar way. The simplest physical description for this comes from the perimeter free electron orbital (PFEO) theory,^{1,58} which models the π electrons as being confined in an oval-shaped infinite potential with no other electron–nuclear or electron–electron interactions. This leads to a particle-on-a-ring wave function for each π electron; a particular electronic state is then characterized by the total ring quantum number Q , which is the sum of the individual ring quantum numbers. The number of nodal planes

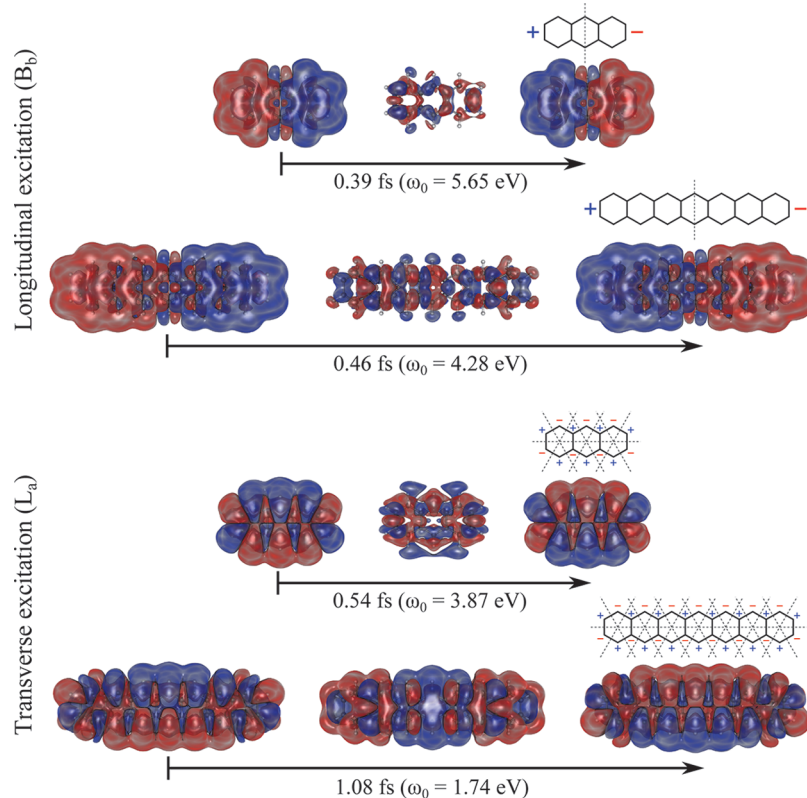


Figure 4. Real-time TDDFT (6-31G**/BNL) isosurface snapshots of the deviation of the charge density from the ground state for anthracene ($N = 3$) and heptacene ($N = 7$), after resonant excitation (frequencies shown in eV). Positive deviation (more charge density than in the ground state) is shown in blue, while negative deviation (less charge density than ground state) is shown in red. The time for a charge oscillation (half period) is shown in femtoseconds. The longitudinal B_b state (note: not compared in Table 1) is covalent in nature. The ionic character of the L_a state is clearly visible from the alternation of charge buildup above/below the C–H bonds and charge depletion on the carbon atoms between. The corresponding perimeter free electron orbital (PFEO) theory structures are shown, confirming that the excited state densities at the oscillation maxima are extremely similar to those arising from π electrons confined to a ring. The densities were visualized using Blender.⁵⁹

for a particular state is then Q , with alternating positive and negative charge buildup at each antinode. This is clearly visible in Figure 4, where the charge density deviations at the maxima of the oscillations (i.e., the excited electronic states) directly match up to the PFE0 predictions. In anthracene, for example, the excited state charge density of the B_b state corresponds to a $Q = 1$ state (one node; high longitudinal dipole moment), whereas the L_a state corresponds to $Q = 7$ (seven nodes; low but nonzero transverse dipole moment). The transition to $Q = 7$ (L_a) requires less energy than that to $Q = 1$ (B_b), which is a consequence of Hund's rule.¹ Larger acenes have larger circumferences, and thus their excitation energies are red-shifted.

4. CONCLUSIONS

In summary, we have computed the L_a and L_b vertical excitation energies for the acenes ranging from anthracene to heptacene, using a broad spectrum of excited-state theoretical approaches. High accuracy coupled cluster calculations (CR-EOMCCST(T)) agree extremely well with experimental results for both states and thus serve as a baseline for validating the lower level theories. Global hybrid TDDFT (e.g. B3LYP) performs poorly for the L_a state, as expected, whereas range-separated hybrid (RSH) TDDFT (e.g. CAM-B3LYP, LC-BLYP, etc) better describes the ionic L_a state, at a cost of lost accuracy for the L_b state. Real-time RSH TDDFT visualization shows that the excited state charge densities are consistent with the predictions of perimeter free electron orbital (PFE0) theory, and the red shifts of the excitations are due to particle-on-a-ring-like confinements. For the semiempirical methods, with proper parametrization, ZINDO rivals range-separated hybrids in accuracy, at a fraction of the computational cost. This suggests a multitiered approach to modeling complicated acene derivatives, as well films and crystals of these molecules: high accuracy coupled cluster calculations validate RSH TDDFT calculations on small (perhaps pairs of) molecules, which in turn enables careful parametrization of semiempirical calculations capable of modeling large systems.

AUTHOR INFORMATION

Corresponding Author

*E-mail: kenneth.lopat@pnnl.gov; dxn@chem.ucla.edu; niri.govind@pnnl.gov; karol.kowalski@pnnl.gov.

ACKNOWLEDGMENT

A portion of the research was performed using EMSL, a national scientific user facility sponsored by the U.S. Department of Energy's Office of Biological and Environmental Research and located at Pacific Northwest National Laboratory (PNNL). PNNL is operated for the Department of Energy by the Battelle Memorial Institute under Contract DE-AC06-76RLO-1830. K.L. acknowledges the William Wiley Postdoctoral Fellowship from EMSL. K.K. and N.G. acknowledge support from the Extreme Scale Computing Initiative, a Laboratory Directed Research and Development Program at Pacific Northwest National Laboratory. D.N. and R.R. gratefully acknowledge support by DOE-EFRC.

REFERENCES

(1) Pope, M.; Swenberg, C. E. *Electronic processes in organic crystals and polymers*, 2nd ed.; Oxford University Press: Oxford, U.K., 1999; Chapter 1, pp 7–12.

- (2) Picciolo, L. C.; Murata, H.; Kafafi, Z. H. *Appl. Phys. Lett.* **2001**, *78*, 2378.
- (3) Wolak, M. A.; Jang, B. B.; Palilis, L. C.; Kafafi, Z. H. *J. Phys. Chem. B* **2004**, *108*, 5492–5499.
- (4) Xu, Q.; Duong, H. M.; Wudl, F.; Yang, Y. *Appl. Phys. Lett.* **2004**, *85*, 3357.
- (5) Lin, C. Y.; Wang, Y. C.; Hsu, S. J.; Lo, C. F.; Diao, E. W. *J. Phys. Chem. C* **2009**, *114*, 687–693.
- (6) Lloyd, M. T.; Mayer, A. C.; Subramanian, S.; Mourey, D. A.; Herman, D. J.; Bapat, A. V.; Anthony, J. E.; Malliaras, G. G. *J. Am. Chem. Soc.* **2007**, *129*, 9144–9149.
- (7) Jiang, Y.; Okamoto, T.; Becerril, H. A.; Hong, S.; Tang, M. L.; Mayer, A. C.; Parmer, J. E.; McGehee, M. D.; Bao, Z. *Macromolecules* **2010**, *42*, 6361–6367.
- (8) Sheraw, C. D.; Zhou, L.; Huang, J. R.; Gundlach, D. J.; Jackson, T. N.; Kane, M. G.; Hill, I. G.; Hammond, M. S.; Campi, J.; Greening, B. K.; Francl, J.; West, J. *Appl. Phys. Lett.* **2002**, *80*, 1088–1090.
- (9) Merlo, J. A.; Newman, C. R.; Gerlach, C. P.; Kelley, T. W.; Muires, D. V.; Fritz, S. E.; Toney, M. F.; Frisbie, C. D. *J. Am. Chem. Soc.* **2005**, *127*, 3997–4009.
- (10) Tang, M. L.; Reichardt, A. D.; Miyaki, N.; Stoltenberg, R. M.; Bao, Z. *J. Am. Chem. Soc.* **2008**, *130*, 6064–6065.
- (11) Lin, Y. Y.; Gundlach, D. J.; Nelson, S. F.; Jackson, T. N. *Electron Device Lett., IEEE* **1997**, *18*, 606–608.
- (12) Klauk, H.; Halik, M.; Zschieschang, U.; Schmid, G.; Radlik, W.; Weber, W. *J. Appl. Phys.* **2002**, *92*, 5259.
- (13) Kim, G. H.; Shtein, M.; Pipe, K. P. *Appl. Phys. Lett.* **2011**, *98*, 093303.
- (14) Anthony, J. E. *Chem. Rev.* **2006**, *106*, 5028–5048.
- (15) Anthony, J. E. *Angew. Chem., Int. Ed.* **2008**, *47*, 452–483.
- (16) Kawashima, Y.; Hashimoto, T.; Nakano, H.; Hirao, K. *Theor. Chem. Acc.* **1999**, *102*, 49–64.
- (17) Wong, B. M.; Hsieh, T. H. *J. Chem. Theory Comput.* **2010**, *6*, 3704–3712.
- (18) Richard, R. M.; Herbert, J. M. *J. Chem. Theory Comput.* **2011**, *7*, 1296–1306.
- (19) Kuritz, N.; Stein, T.; Baer, R.; Kronik, L. *J. Chem. Theory Comput.* **2011**, *7*, 2408–2415.
- (20) Grimme, S.; Parac, M. *ChemPhysChem* **2003**, *4*, 292–295.
- (21) Bak, K. L.; Koch, H.; Oddershede, J.; Christiansen, O.; Sauer, S. P. A. *J. Chem. Phys.* **2000**, *112*, 4173–4185.
- (22) Peach, M. J. G.; Benfield, P.; Helgaker, T.; Tozer, D. J. *J. Chem. Phys.* **2008**, *128*, 044118.
- (23) Huang, L.; Rocca, D.; Baroni, S.; Gubbins, K. E.; Nardelli, M. B. *J. Chem. Phys.* **2009**, *130*, 194701.
- (24) Runge, E.; Gross, E. K. U. *Phys. Rev. Lett.* **1984**, *52*, 997.
- (25) Petersilka, M.; Gossmann, U. J.; Gross, E. K. U. *Phys. Rev. Lett.* **1996**, *76*, 1212–1215.
- (26) Casida, M. E. In *Recent Advances in Density Functional Methods*; Chong, D. P., Ed.; World Scientific Publishing: River Edge, NJ, 1995; Vol. 1, Chapter 5, pp 155–192.
- (27) Valiev, M.; Bylaska, E. J.; Govind, N.; Kowalski, K.; Straatsma, T. P.; Van Dam, H. J. J.; Wang, D.; Nieplocha, J.; Apra, E.; Windus, T. L.; de Jong, W. A. *Comput. Phys. Commun.* **2010**, *181*, 1477–1489.
- (28) Stewart, J. J. P. *J. Comput. Chem.* **1989**, *10*, 209–220.
- (29) MOPAC 6.0. <http://ccl.net/cca/software/MS-WIN95-NT/mopac6/index.shtml> (accessed September 2011).
- (30) Bartell, L. A.; Wall, M. R.; Neuhauser, D. *J. Chem. Phys.* **2010**, *132*, 234106.
- (31) Zerner, M. C. et al. *ZINDO-MN*, version 2011; Quantum Theory Project, University of Florida: Gainesville, FL; Department of Chemistry, University of Minnesota: Minneapolis, MN, 2011.
- (32) Hirata, S.; Head-Gordon, M. *Chem. Phys. Lett.* **1999**, *302*, 375–382.
- (33) Bartlett, R. J.; Musiał, M. *Rev. Mod. Phys.* **2007**, *79*, 291–352.
- (34) Kowalski, K.; Krishnamoorthy, S.; Villa, O.; Hammond, J. R.; Govind, N. *J. Chem. Phys.* **2010**, *132*, 154103.
- (35) Watts, J. D.; Bartlett, R. J. *J. Chem. Phys. Lett.* **1995**, *233*, 81–87.

- (36) Watts, J. D.; Bartlett, R. J. *Chem. Phys. Lett.* **1996**, *258*, 581–588.
- (37) Christiansen, O.; Koch, H.; Jørgensen, P. *J. Chem. Phys.* **1996**, *105*, 1451.
- (38) Hirata, S.; Nooijen, M.; Grabowski, I.; Bartlett, R. J. *J. Chem. Phys.* **2001**, *114*, 3919.
- (39) Shiozaki, T.; Hirao, K.; Hirata, S. *J. Chem. Phys.* **2007**, *126*, 244106.
- (40) Manohar, P. U.; Krylov, A. I. *J. Chem. Phys.* **2008**, *129*, 194105.
- (41) Kowalski, K.; Piecuch, P. *J. Chem. Phys.* **2004**, *120*, 1715.
- (42) Kowalski, K.; Piecuch, P. *J. Chem. Phys.* **2001**, *115*, 2966.
- (43) Włoch, M.; Lodriguito, M. D.; Piecuch, P.; Gour, J. R. *Mol. Phys.* **2006**, *104*, 2991.
- (44) Piecuch, P.; Gour, J. R.; Włoch, M. *Int. J. Quantum Chem.* **2009**, *109*, 3268–3304.
- (45) Kowalski, K. *J. Chem. Phys.* **2009**, *130*, 194110.
- (46) Raghavachari, K.; Trucks, G. W.; Pople, J. A.; Head-Gordon, M. *Chem. Phys. Lett.* **1989**, *157*, 479–483.
- (47) Lopata, K.; Govind, N. *J. Chem. Theory Comput.* **2011**, *7*, 1344–1355.
- (48) Anderson, W. P.; Cundari, T. R.; Zerner, M. C. *Int. J. Quantum Chem.* **1991**, *39*, 31–45.
- (49) Stephens, P. J.; Devlin, F. J.; Chabalowski, C. F.; Frisch, M. J. *J. Phys. Chem.* **1994**, *98*, 11623–11627.
- (50) Yanai, T.; Tew, D. P.; Handy, N. C. *Chem. Phys. Lett.* **2004**, *393*, 51–57.
- (51) Rohrdanz, M. A.; Martins, K. M.; Herbert, J. M. *J. Chem. Phys.* **2009**, *130*, 054112.
- (52) Baer, R.; Neuhauser, D. *Phys. Rev. Lett.* **2005**, *94*, 043002.
- (53) Lambert, W. R.; Felker, P. M.; Syage, J. A.; Zewail, A. H. *J. Chem. Phys.* **1984**, *81*, 2195.
- (54) Hirao, K. *Chem. Phys. Lett.* **1992**, *190*, 374–380.
- (55) Hirao, K. *Chem. Phys. Lett.* **1992**, *196*, 397–403.
- (56) Christiansen, O.; Koch, H.; Jørgensen, P. *Chem. Phys. Lett.* **1995**, *243*, 409–418.
- (57) Baer, R.; Livshits, E.; Salzner, U. *Annu. Rev. Phys. Chem.* **2010**, *61*, 85–109.
- (58) Platt, J. R. *J. Chem. Phys.* **1949**, *17*, 484–495.
- (59) *Blender*; The Blender Foundation: Amsterdam, The Netherlands, 2010.